# Parametric study of laser wakefield driven generation of intense sub-cycle pulses

(article starts on next page)

**PAPER • OPEN ACCESS**

# Parametric study of laser wakefield driven generation of intense sub-cycle pulses

To cite this article: E Siminos and I Thiele 2022 *Plasma Phys. Control. Fusion* **64** 034006

View the article online for updates and enhancements.

# Parametric study of laser wakefield driven generation of intense sub-cycle pulses

## E Siminos[1,*] and I Thiele[2]

[1] Department of Physics, University of Gothenburg, SE-412 96 Göteborg, Sweden
[2] Department of Physics, Chalmers University of Technology, SE-412 96 Göteborg, Sweden

E-mail: evangelos.siminos@gmail.com

CrossMark

## Abstract

Intense sub-cycle electromagnetic pulses allow one to drive nonlinear processes in matter with unprecedented levels of control. However, it remains challenging to scale such sources in the relativistic regime. Recently, a scheme that utilizes laser-driven wakes in plasmas to amplify and compress seed laser pulses to produce tunable, carrier-envelope-phase stable, relativistic sub-cycle pulses has been proposed. Here, we present parametric studies of this process using particle-in-cell simulations, showing its robustness over a wide range of experimentally accessible laser-plasma interaction parameters, spanning more than two orders of magnitude of background plasma density. The method is shown to work with different gas-jet profiles, including structured density profiles and is robust over a relatively wide range of driver laser intensities. Our study shows that sub-cycle pulses of up to 10mJ of energy can be produced.

Keywords: laser-plasma interaction, sub-cycle plasma, laser-wakefield acceleration

(Some figures may appear in colour only in the online journal)

## 1. Introduction

Generation of few-cycle electromagnetic pulses has steadily advanced, driven by applications that require probing or control of ultra-fast processes [1–4]. Recently, a lot of effort has been devoted to produce sub-cycle pulses in which the time-envelope is modulated on a time scale shorter than a single cycle. Such pulses bring temporal resolution to its ultimate limits and are unique tools for the control of electron motion in solids [5, 6], electron tunnelling in nano-devices [7, 8], reaction dynamics at the electronic level [9], as well as the generation of isolated attosecond and zeptosecond x-ray pulses [10, 11]. Several methods have been developed for the generation of sub-cycle pulses from the THz to x-ray regimes, see the review [12]. However, scaling such methods towards high intensities remains challenging and thus is a field of active research, in particular in the mid-infrared regime, where intense sub-cycle pulses are very attractive for applications [13, 14].

Plasma-based methods, which could scale to relativistic intensities, offer the possibility to work past the limitations of conventional schemes. Much of the work on such methods has focussed on attosecond pulse generation in the extreme ultraviolet (XUV) regime, with several techniques being developed in order to produce isolated pulses, such as polarization [15–17] or intensity gating [18–21] and wavefront rotation [22, 23]. In the long-wavelength limit, plasma-based methods have been proposed to generate mid-infrared (mid-IR), single and sub-cycle pulses. As an example, we have proposed that electron beams can be used to generate intense sub-cycle pulses, by amplifying a seed pulse reflected

---

* Author to whom any correspondence should be addressed.

by a foil [24]. A different technique for mid-IR near-single-cycle pulses utilizing laser frequency down-conversion in laser-driven wakefields, has been proposed in [25] and experimentally demonstrated in [26]. However, all aforementioned plasma-based techniques are either not CEP-tunable or require a controllable CEP-stable high-intensity laser, which is technically challenging.

In a recent article [27], we proposed a new frequency upconversion process, referred to as laser-wakefield driven amplification (LWDA), which can be used to generate isolated carrier-envelope-phase (CEP)-tunable intense sub-cycle pulses. It involves injecting a CEP-stable long-wavelength seed pulse of relatively low intensity in co-propagation with a relativistically intense, not necessarily CEP-stable, driver laser pulse into a gas jet. The relativistic pulse creates an underdense plasma, in which it drives a plasma wake. In the non-linear wake regime, the first electron density spike of the wake is most pronounced and can be used to amplify and compress the co-propagating seed pulse up to relativistic amplitude and sub-cycle pulse duration, see figure 1. In this work we present a detailed parametric study of the LWDA process, focused around the choice of plasma parameters, in particular ambient plasma density and gas jet length and profile. This allows us to elaborate on the experimental feasibility of the scheme as well as the choice of optimal parameters.

## 2. Simulation of LWDA

When a high-intensity laser travels through a gas-jet, it creates a wakefield containing electron density spikes moving with almost the speed of light. This non-stationary electron density structure can amplify a co-propagating electromagnetic field. This process is illustrated here using 2D and 3D Particle-in-Cell (PIC) simulations, performed with the high-performance open-source code SMILEI [28]. For the electromagnetic fields, we have employed the Yee scheme in Cartesian coordinates and the Silver-Müller boundary conditions. In 2D, the longitudinal mesh-size $\delta_x = 16$ nm, the transverse mesh size $\delta_y = 32$ nm and a temporal step $\delta_t = 47$ as were used. Here, we assumed translational invariance along the $z$ direction. In 3D, the longitudinal mesh-size $\delta_x = 16$ nm, the transverse mesh sizes $\delta_y = 32$ nm and $\delta_z = 32$ nm as well as a temporal step $\delta_t = 42$ as were used. For the electrons, we have employed the relativistic Boris pusher, while the ions were assumed to be fixed. The background plasma profile in most simulations was assumed as a flat-top of density $n_0$ (the effect of Gaussian and structured plasma profiles is studied in section 3.4). In 2D, we have initialized 100 macro-particles per cell. In 3D, the number of macro-particles per cell was reduced to 10.

A $y$-polarized driving laser pulse and a $z$-polarized seed pulse are injected to propagate along the $x$ direction and are defined by their transverse electric field components $E_{y,L}$ and $E_{z,S}$ respectively, at the entrance of the gas-jet according to

$$E_{y/z,L/S}(\mathbf{r}_\perp, t) = E_{0,L/S} f_\perp(\mathbf{r}_\perp) \sin\left(\omega_{L/S} t + \phi_{L/S}\right) f_{L/S}(t),$$
(1)

with the amplitudes $E_{0,L/S}$, transverse profiles $f_\perp(\mathbf{r}_\perp) = \exp\left(-\mathbf{r}_\perp^2/r_{0,L/S}^2\right)$, beam waists $r_{0,L/S}$, angular frequencies $\omega_{0,L/S}$ and phases $\phi_S$ and $\phi_L = 0$. For the driver laser and the seed in the pulsed case, we use an envelope of the form $f(t) = \exp\left(-2\ln(2)\, t^2/t_{0,L/S}^2\right)$. The algorithm presented in [29, 30] is used in order to obtain the laser electric fields according to equation (1) at the entrance of the gas jet in the PIC simulations.

We demonstrate sub-cycle pulse generation by means of a 3D PIC simulation (see figure 1). We consider a 39 mJ, 10 fs long, 800 nm driver pulse with a 2.5 $\mu$m focal spot. This corresponds to a peak electric field $E_{0,L} = 100$ GV cm$^{-1}$ or a normalized peak vector potential $a_{0,L} = q_e A_{0,L}/m_e c = 2.5$ (a pulse is relativistic if $a_{0,L} \gtrsim 1$). The seed pulse is moderately intense ($E_{0,S} = 4$ GV cm$^{-1}$), with 4 $\mu$m wavelength and a 5 $\mu$m focal spot, in the continuous wave (CW) approximation. To model a gas-jet of length $L_p$, we assume a plasma with electron density $n_e = 4.5 \cdot 10^{19}$ cm$^{-3}$.

Figure 1(a) shows how the first electron density spike of the wake behind the laser pulse amplifies the seed pulse and forms a sub-cycle pulse. The second and subsequent electron density spikes also create sub-cycle pulses (see figure 1(b)). However, these have an intensity at least one order of magnitude smaller than that of the leading pulse, which is amplified by the dominant electron density spike. The maximum electric field of the amplified seed is increased by a factor of 16, compared to the initial electric field amplitude. This is enough to accelerate the plasma electrons above 10% of the speed of light. While for a short propagation distance, the electron density profile in the wake would be expected to remain cylindrically symmetric [31], the relativistic sub-cycle pulse deforms it, introducing an asymmetry, which can be seen in figure 1(b). The sub-cycle pulse exits the plasma with an ultra-broad spectrum peaked around 1.2 $\mu$m (260 THz, 3.5-times larger than the central frequency of the seed, see figures 1(c) and (d)), an intensity FWHM duration of $\sim$3 fs or 0.8 cycles and polarization orthogonal to the pump. The latter property allows the sub-cycle and pump pulses to be separated after the interaction.

The amplification mechanism has been studied using a 1D relativistic, Maxwell fluid model in [27], which we briefly review. The propagation of the seed in the plasma is described by the wave equation

$$\partial_{xx}^2 A_z - \partial_{tt}^2 A_z = n_e A_z/\gamma_e = n_0 A_z/(1 + \phi),$$
(2)

where $\phi$, $n_e$ and $\gamma_e$ are the wake scalar potential, electron fluid density and relativistic factor respectively, $A_z$ is the seed vector potential and $n_0$ the background plasma density. Here, we use relativistic units: velocity, time, and distance are normalized to the speed of light in vacuum $c$, inverse driver laser frequency $\omega_{L,0}^{-1}$, and inverse vacuum driver laser wave number $k_L^{-1} = c/\omega_{L,0}$ respectively. Electric charges and masses are normalized to $e$ and $m_e$ respectively and densities are normalized to the critical density $n_c = \epsilon_0 m_e \omega_{0,L}^2/q_e^2$, while electric fields are normalized to the Compton field $E_C = m_e c \omega_L/e$. In the last step of equation (2), use has been made of the fact that, in
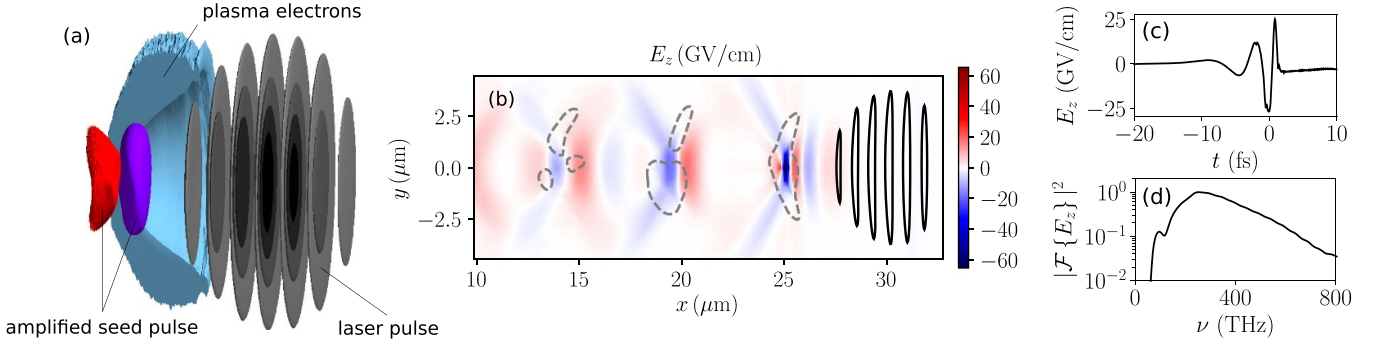
**Figure 1.** (a) Illustration of LWDA using a 3D particle-in-cell simulation, (b) a cross-section of the amplified seed electric field $E_z$ in the $xy$-plane with contour lines of the electron density $n_e(x,y) = 0.15 \max n_e$ (dashed lines) and the laser electric field $E_y(x,y) = \max E_y/4$ (solid lines), (c) on-axis electric field of the sub-cycle pulse 8 $\mu$m past the exit of the gas-jet and (d) the corresponding spectrum. The simulation parameters are $E_{0,L} = 100$ GV cm$^{-1}$, $\lambda_L = 0.8$ $\mu$m, $t_{0,L} = 9.8$ fs, $\phi_L = 0$, $r_{0,L} = 4.2$ $\mu$m, $E_{0,S} = 4$ GV cm$^{-1}$, $\lambda_S = 4$ $\mu$m, $t_{0,S} = \infty$ (CW), $\phi_S = 0$, $r_{0,S} = 5$ $\mu$m, $n_e = 4.5 \cdot 10^{19}$ cm$^{-3}$ and $L_p = 23$ $\mu$m (see text for details).

the quasistatic approximation for the driver laser, propagation $n_e/\gamma_e = n_0/(1 + \phi)$ [32]. The scalar potential for the nonlinear wake is determined by numerically solving [32–34]

$$\frac{d^2\phi}{d\xi^2} = n_0 \left( \frac{1 + A_y^2}{2(1 + \phi)^2} - \frac{1}{2} \right), \qquad (3)$$

where $A_y$ is the vector potential of the driver laser, $\xi = x - v_g t$ and $v_g \simeq c(1 - 1.5\,n_0/n_c)$ is the driver group velocity [35]. The solution of equation (3) for $\phi$ is used in order to solve equation (2) numerically. The model predicts rapid seed wavelength decrease, as well as a significant electromagnetic field energy gain associated with localized amplification at the front of the density spike of the wake [27]. This is consistent with the prediction of [24], that a pulse can gain energy from the declining part (with respect to $x$) of a sub-wavelength, moving density perturbation. The frequency up-shift is primarily caused by the short duration of the amplifying electron density peak and should not be confused with the 'photon acceleration' mechanism [36–40] which occurs when a many-cycle pulse is frequency up-shifted by a moving electron density up-ramp, which changes slowly compared to the seed pulse duration. At a fundamental level, seed amplification could seem as subwavelength coherent synchrotron emission (CSE), caused by the quivering of the moving electron distribution in the seed electromagnetic field. However, it was shown in [41] that considering a CSE-type effect, which does not self-consistently take into account propagation effects of the seed in the wakefield structure does not correctly reproduce the amplified pulse waveform. The cold-fluid model of equations (2) and (3) has been proposed as a minimal model that captures the main characteristics of the amplification process [27].

## 3. Parametric scans

### 3.1. Comparison of 3D and 2D results

In order to determine the optimal interaction regime, we perform an extensive parametric study, with 2D rather than 3D simulations. Here, we recall certain aspects of the comparison
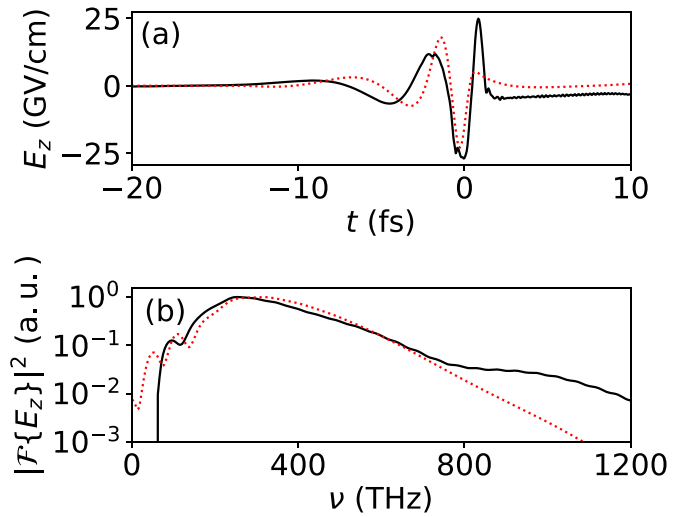


**Figure 2.** Comparison of (a) sub-cycle pulse and (b) corresponding spectra, obtained by a 3D (solid black line) and 2D (dotted red line) PIC simulation for the parameters of figure 1. Reproduced from [27]. CC BY 4.0.

of 2D and 3D simulations discussed in the supplemental material of [27]. In order to demonstrate that this approach can provide a qualitatively correct picture of the parameter dependence, we present a direct comparison of the sub-cycle waveforms and spectra in 2D and 3D simulations in figure 2. The parameters are the same as in figure 1. Since the seed pulse reaches relativistic amplitude, the interaction is nonlinear and this leads to a worst-case scenario for comparison of 2D and 3D results. Figure 2 shows that both the amplitude of the sub-cycle pulse, as well as its central frequency and most of the spectrum, are reproduced relatively well by 2D simulations. The main difference is in the presence of a high-frequency tail in 3D, consistent with a more pronounced density spike due to more efficient relativistic self-focusing in 3D than in 2D, see also the discussion of figure 7. On the other hand, the spectrum decays faster for frequencies close to zero in 3D than in 2D. This discrepancy in 2D is related to the fact that fields decay more slowly in a 2D approximation. However, both ends of
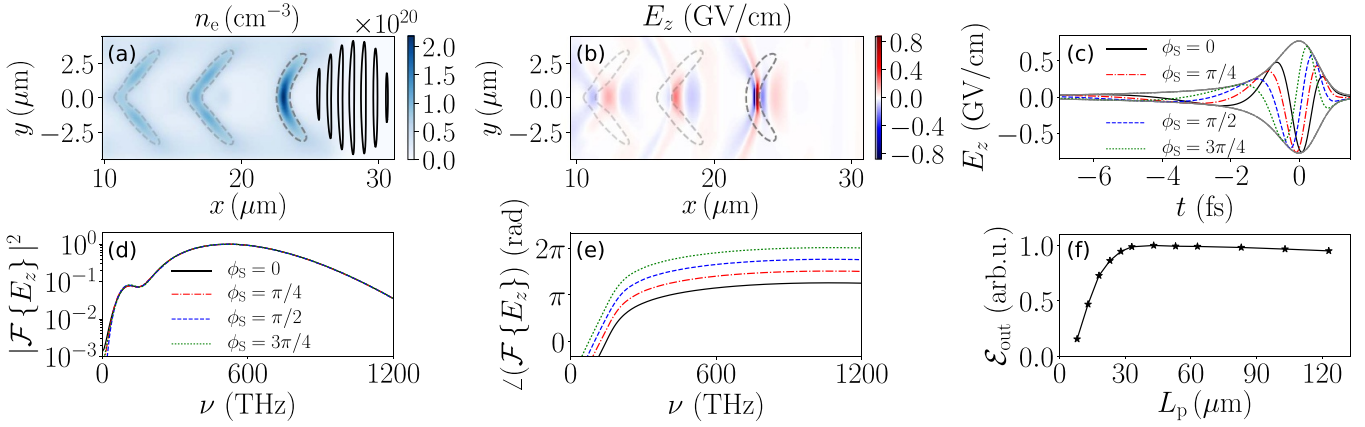
**Figure 3.** Results of 2D PIC simulations using a weak seed pulse with $E_{0,\mathrm{S}} = 0.04$ GV cm$^{-1}$: (a) electron density with contours at $n_{\mathrm{e}}(x,y) = \max n_{\mathrm{e}}/3$ (dashed lines) and contours of the laser electric field $E_y(x,y) = \max E_y/4$ (solid lines), (b) amplified seed electric field $E_z$ with electron density contours, (c) on-axis electric fields of the amplified sub-cycle pulses after the interaction for different seed CEPs $\phi_{\mathrm{S}}$ and their common envelope (gray line), (d) corresponding power spectrum and (e) spectral phase, (f) plasma-length $L_{\mathrm{p}}$ dependency of the sub-cycle pulse energy. The simulation parameters (other than $E_{0,\mathrm{S}}$) are the same as for figure 1. (c), (f) Reproduced from [27].

the spectrum lie outside the spectral range of interest for our sub-cycle pulses, which is limited to about 2.5 octaves around the central frequency, see figure 9.

It is also important to compare differences in energy conversion efficiency, which we take to be the ratio of sub-cycle to drive-laser energy (note that in 2D 'energy' has units of energy per unit length). The conversion efficiency would scale with dimension $d$ as [27]

$$\eta \sim \left(\frac{E_{\mathrm{sub},0}}{E_{L,0}}\right)^2 \left(\frac{r_{\mathrm{sub},0}}{r_{L,0}}\right)^{d-1} \frac{t_{\mathrm{sub},0}}{t_{L,0}}, \tag{4}$$

where $E_{\mathrm{sub},0}$ ($E_{L,0}$), $r_{\mathrm{sub},0}$ ($r_{L,0}$) and $t_{\mathrm{sub},0}$ ($t_{L,0}$) are the subcycle (drive laser) maximum field, waist and duration respectively. While the explicit dependence on dimensionality in the second term would suggest that conversion efficiency would be overestimated in 2D, one needs to take into account that there is also implicit dependence through the output sub-cycle field $E_{\mathrm{sub},0}$ and duration $t_{\mathrm{sub},0}$, which are both slightly higher in 3D (see figure 2). By evaluating conversion efficiency for the simulations of figure 2 (after spectral filtering to retain 2.5 octaves around the central wavelength) we find that $\eta \sim 0.3\%$ in both 2D and 3D.

For the purpose of performing parametric scans to illustrate the dependencies of LWDA on various parameters, 2D simulations are thus deemed adequate, since they capture the main features of interest.

### 3.2. Effect of basic laser-plasma parameters

As a reference case for our parametric studies, we take the simulation presented in figure 3(a), in which the parameters are the same as for the simulation shown in figure 1, apart from the lower amplitude of the seed. The choice of a lower seed amplitude has been made in order to simplify the parametric study by eliminating nonlinear effects due to the seed reaching relativistic amplitude after amplification. All

parameters not mentioned explicitly in the following studies are assumed to be the same as in figure 3(a) and the geometry in all remaining simulations is two-dimensional. The electron density in figure 3(a) remains symmetric and the wake remains almost unperturbed by the seed pulse. The seed electric field, shown in figure 3(b), is increased by a factor of 19. As shown below, for sufficiently low initial seed amplitudes, this amplification factor remains constant with respect to the initial seed amplitude. The sub-cycle pulse (see figure 3(c)) has an ultra-broad spectrum, which is peaked around 520 THz (0.6 $\mu$m), 7-times larger than the central frequency of the seed (see figure 3(d)), while its intensity FWHM duration is equivalent to 0.53 cycles.

In order to tune the CEP of the sub-cycle pulse, it is sufficient to change the CEP of the many-cycle seed pulse, or to delay it with respect to the laser pulse. Figure 3(c) presents the on-axis electric field shapes after the interaction using four different seed pulse CEPs $\phi_{\mathrm{S}}$. It can be seen that the sub-cycle pulse envelopes are the same, as are the power spectra of the pulses (see figure 3(d)). However, the phases of the sub-cycle pulses are shifted by a value of $\pi/4$, exactly the same as for the seed. This is shown in the frequency domain by presenting the spectral phases in figure 3(e).

A delay of the seed pulse with respect to the driving laser pulse can also be used to tune the seed pulse CEP. This is possible for sufficiently long seed pulses, where variation of the CEP and the delay lead to almost the same seed-pulse up to terms of order $1/(\omega_{\mathrm{S}} t_{0,\mathrm{S}})$. The synchronization level necessary to achieve a change of $\pi/2$ in CEP is $\lambda_{\mathrm{S}}/4$. For the range of densities studied here, this corresponds to 3–17 fs, which is within present experimental capabilities [42].

According to figure 3(f), which shows the sub-cycle pulse energy $\mathcal{E}_{\mathrm{out}}$ versus the gas-jet length $L_{\mathrm{p}}$, the amplification takes place during the first 30 $\mu$m of propagation. There are two factors contributing to the relatively short distance over which amplification occurs. First, once the seed pulse frequency upshifts, its group velocity increases and the amplified seed
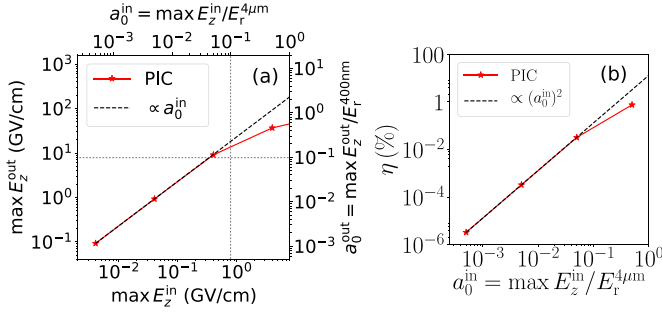
**Figure 4.** (a) Peak electric fields of the sub-cycle pulse and (b) conversion efficiency dependence on the peak seed electric field. The remaining parameters of the 2D PIC simulations are the same as in figure 3. In (a) two scales are provided; one in SI units and another in relativistic units demonstrating the generation of relativistically strong sub-cycle pulses. In addition, the dashed lines present the scaling expected for weak seed pulses. Reproduced from [27].
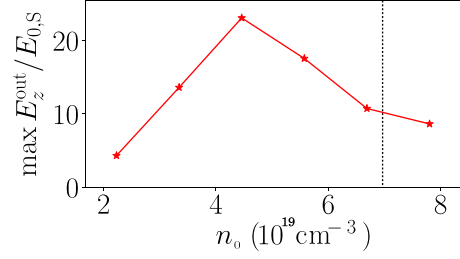


**Figure 5.** Peak electric field of the sub-cycle pulses normalized to the seed electric field depending on background electron density from 2D PIC simulation. The other parameters are the same as in figure 3. The dotted line marks the critical density $n_{c,S}$ for the 4 $\mu$m seed pulse.

moves into a low density region in the wake. This has been corroborated by the 1D relativistic fluid model study in [27]. Second, in 2D and 3D simulations, relativistic self-focusing of the laser pulse leads to bubble lengthening and wavebreaking [31, 43, 44] which can also cause amplification to cease. After wavebreaking, the sub-cycle pulse is guided inside the bubble for distances of up to the driver depletion length $L_{pd} \propto \lambda_{pe}^3/\lambda_L^2$ [45]. For the present parameters, our simulations show that the pump is able to drive a bubble for about 200 $\mu$m of propagation. It was found that the extended interaction length afforded due to the absence of wavebreaking in 1D fluid simulations led to longer amplified pulses. One could therefore utilize wavebreaking through a density downramp [46–48] in Gaussian density profiles of realistic dimensions [47, 49] as a means to keep the sub-cycle duration as short as possible. We discuss this strategy in detail in section 3.4.

The 1D model of [27] predicts a linear scaling of the sub-cycle electric field amplitude with the seed electric field amplitude. Our 2D PIC simulation results, which are presented in figure 4(a), confirm this prediction up to weakly relativistic seed pulse amplitudes. To judge how relativistic the seed and sub-cycle pulses are, this figure contains, besides the maximum electric field strengths in SI units, the field strength scaled by the relativistic electric field $E_r^\lambda = 2\pi c^2 m_e/(q_e \lambda)$, which characterizes, for a given wavelength $\lambda$, the field strength at which a free electron would be accelerated to almost the speed of light. This normalization employs the central wavelengths of the seed and sub-cycle pulses, respectively. Figure 4(a) reveals that using weakly relativistic seed pulses ($a_0^{in} = \max E_z^{in}/E_r^\lambda \sim 0.1$), weakly relativistic sub-cycle pulses ($a_0^{out} = \max E_z^{out}/E_r^\lambda \sim 0.25$) can be obtained. The suboptimal scaling for $a_0^{in} > 0.1$ is caused by the distortion of the wake by the generated intense sub-cycle pulse. In this case, the wake electrons lose a substantial fraction of their energy to the seed pulse and the wake structure cannot be considered to be independent of the sub-cycle electric field $E_z$ anymore. Figure 4(b) shows that the laser-to-sub-cycle-pulse conversion efficiency $\eta$ reaches about 1% for $n_0 = 4.5 \cdot 10^{-19}$ cm$^{-3}$.

In order to study the scaling with the background electron density, we perform two different kinds of parameter studies. In figure 5, we vary the electron density, keeping all other simulation parameters fixed. The dashed line specifies the critical density $n_{c,S} = \epsilon_0 m_e \omega_S^2/q_e^2$ at which the plasma becomes opaque for the seed pulse. Two counter-acting effects lead to an optimal value of initial electron density smaller than $n_{c,S}$: An increase of the electron density leads, according to [27], to stronger amplification However, it also leads to reduced penetration of the seed pulse into the plasma.

In order to scale our results across background electron densities different by more than an order of magnitude, we observe that, for a given driving laser amplitude $a_{0,L}$, the interaction is determined by the ratio of the laser wavelength $\lambda_L$ to the plasma wavelength $\lambda_{pe}$, which is in turn determined by the ratio of the electron density $n_0$ to the critical density $n_c$. Here, we fix the laser wavelength to $\lambda_L = 0.8$ $\mu$m and vary $n_0/n_c$, while we scale all other parameters in proportion to the plasma wavelength. In particular, for the density scan of figure 6(a), the simulation parameters have been chosen as $E_{0,L} = 100$ GV cm$^{-1}$ ($a_{0,L} = 2.5$), $\lambda_L = 0.8$ $\mu$m, $t_{0,L} = \lambda_{pe}/2$, $\phi_L = 0$, $r_{0,L} = 0.83$ $\lambda_{pe}$, $E_{0,S} = 0.04$ GV cm$^{-1}$, $\lambda_S = 0.8$ $\lambda_{pe}$, $t_{0,S} = \infty$ (CW), $\phi_S = 0$, $r_{0,S} = \lambda_{pe}$ and $L_p = 6$ $\lambda_{pe}$. In this way, we ensure propagation of the seed, $\omega_S > \omega_{pe}$, while at the same time guaranteeing that the seed wavelength is longer than the electron skin depth, $\lambda_S > c/\omega_{pe} = \lambda_{pe}/2\pi$, which can be taken as an approximation of the density spike characteristic length. For a gas-jet length of $L_p = 6$ $\lambda_{pe}$ the results are shown in figure 6(a). For these specific interaction parameters, we observe that the amplification factor is optimized for $n_0 = 4.5 \cdot 10^{19}$ cm$^{-3} \simeq 0.026$ $n_c$ (corresponding to the example studied in figure 3). For higher densities, the amplification factor decreases. Our simulations show that this is due to more efficient self-focusing at higher densities, which leads to early wavebreaking, as one would expect based on the scaling of the critical power for relativistic self-focusing, $P_c(\text{GW}) = 17.4 \omega^2/\omega_{pe}^2 = 17.4 n_c/n_0$ [34]. For lower densities, on the other hand, self-focusing proceeds more slowly and wavebreaking does not occur within the duration of the simulations. However, the amplification ratio is lower at lower densities, since the first density spike contains less charge.
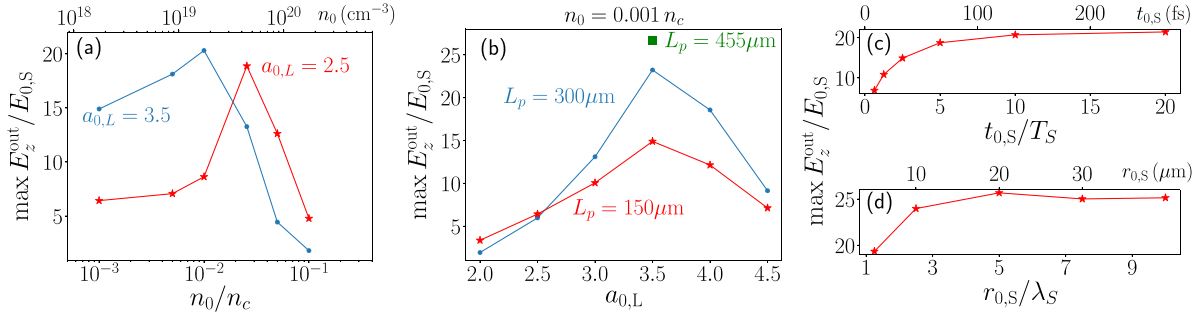
**Figure 6.** 2D PIC simulation results for the peak electric field of the sub-cycle pulses normalized to the seed electric field depending on (a) electron density for two different values of driver amplitude $a_{0,\mathrm{L}} = 2.5$ (red) and $a_{0,\mathrm{L}} = 3.5$ (blue), (b) normalized electric field amplitude, $a_{0,\mathrm{L}}$, of the driving laser for $n_0 = 0.001\,n_\mathrm{c}$ and two different values of the plasma length $L_\mathrm{p}$, (c) the seed pulse duration $t_{0,\mathrm{S}}$ normalized to the seed carrier period $T_\mathrm{S} = c/\lambda_\mathrm{S}$ and (d) the seed waist $r_\mathrm{S}$ normalized to the seed wavelength. In ((a) and (b)) all geometrical parameters (pump waist, gas jet length, etc) and seed wavelength have been rescaled in proportion to the plasma wavelength. In ((c) and (d)) all parameters are the same as in figure 3(a), except $t_{0,\mathrm{S}}$ in (c) and $r_{0,\mathrm{S}}$ in (d).

We note here that the optimal density has been found for fixed driver amplitude $a_{0,\mathrm{L}} = 2.5$. However, relativistic laser-plasma interactions scale (for large $a_{0,\mathrm{L}}$) with the similarity parameter $S = n_0/a_{0,\mathrm{L}}\,n_\mathrm{c}$ [50] and we thus expect that the optimal density would be lower for higher $a_{0,\mathrm{L}}$. This is illustrated in figure 6(a), where we see that for $a_{0,\mathrm{L}} = 3.5$ (blue line) the optimal density is approximately $n_0 = 0.01\,n_\mathrm{c}$.

We will now show that there is further potential for optimization in the low density regime before reaching the wavebreaking threshold. Since accurately capturing the wavebreaking threshold requires 3D simulations, the purpose of our study will be to identify qualitative tendencies when varying different variables, rather than exact optimal parameters. For the lowest density case, $n_0 = 0.001\ n_\mathrm{c} = 1.7 \cdot 10^{18}$ cm$^{-3}$, we illustrate optimization in figure 6(b) where we vary $a_{0,\mathrm{L}}$ for two values of the gas-jet length $L_\mathrm{p} = 6\ \lambda_\mathrm{pe} \simeq 150\ \mu$m and $L_\mathrm{p} = 12\ \lambda_\mathrm{pe} \simeq 300\ \mu$m. We observe that the amplification factor can be increased by increasing $a_{0,\mathrm{L}}$ until $a_{0,\mathrm{L}} > 3.5$, where we are again limited by wavebreaking. For $a_{0,\mathrm{L}} = 3.5$, wavebreaking occurs for a gas-jet length of approximately $L_\mathrm{p} = 18\ \lambda_\mathrm{pe} = 455\ \mu$m (square symbol in figure 6(b)), which is the optimal interaction length for these parameters, leading to an amplification factor of $\sim 27$. Note that in our parametric study, the driver laser pulse duration and waist scale with $\lambda_\mathrm{pe}$ and thus its energy scales as $\lambda_\mathrm{pe}^3$ or $n_0^{-3/2}$. For example, the case with $a_{0,\mathrm{L}} = 3.5$ in figure 6(b) corresponds to a pump duration of 50 fs and energy 10J, focused to a waist of 21 $\mu$m. On the other hand, in these low density simulations, we used longer wavelength (20 $\mu$m) seeds, for which relativistic effects perturb the wake at lower (seed pulse) energies. Therefore, efficiency is limited to 0.1% in this case. Nevertheless, even at this lower conversion efficiency, 10-mJ-strong sub-cycle pulses may be generated using a 10-Joule-class laser driver.

While we have hitherto considered only CW seed pulses, it is possible to use finite duration seed pulses, with Gaussian temporal envelopes as well. This is demonstrated in figure 6(c), which shows the sub-cycle field strength scaling with the seed pulse duration. The amplified field strength reaches saturation for seed pulses longer than ten cycles, while even pulses as short as two or three cycles lead to

amplification by a factor of more than ten. Similarly, we present in figure 6(d) the scaling of the amplification factor as a function of the seed beam waist $r_{0,\mathrm{S}}$. While in most of our simulations we used tightly focused seed beams, with $r_{0,\mathrm{S}} = 1.2\ \lambda_\mathrm{S} = 5\ \mu$m, in order to keep the computational domain as compact as possible, figure 6(d) shows that increasing the beam waist leads to enhanced amplification. The growth of the amplification factor continues up to $r_{0,\mathrm{S}} \sim 5\ \lambda_\mathrm{S} = 20\ \mu$m, beyond which it converges to approximately max $E_z^\mathrm{out}/E_{0,\mathrm{S}} = 25$. Therefore, we can see that the method is very flexible in terms of both seed pulse duration and waist. This eases temporal and spatial overlap requirements, as one can work with a relatively long and wide seed. The main requirement of the seed is that its wavelength is longer and its focal spot wider, than the characteristic length $\sim c/\omega_\mathrm{pe}$ of the density spike. For the pump and plasma parameters of figure 1, a $\lambda_\mathrm{S} = 4\ \mu$m seed of duration 100 fs, focused to a waist of 20 $\mu$m (to achieve optimal amplification according to figures 6(c) and (d)), would correspond to an energy of $\sim 19$ mJ, which is within reach of optical parametric amplification [51].

We now discuss the sub-cycle pulses' shapes and spectra. These are tunable by varying the driver-laser field strength $a_{0,\mathrm{L}}$ and electron density $n_\mathrm{e}$. The larger $a_{0,\mathrm{L}}$ and $n_\mathrm{e}$ are, the narrower the amplifying electron density spikes, which naturally leads to shorter wavelength components in the sub-cycle pulse spectra. Both the central wavelength and the wavelength range can be tuned as shown in figure 7. Reducing the electron density (keeping all other parameters fixed) shifts the sub-cycle pulse peak wavelength towards the mid-IR, while increasing the density shifts it towards the ultraviolet (UV) (see figure 7(c)). By using more intense driver laser pulses, we can introduce shorter wavelength components in the spectra (see figure 7(d)). However due to the breaking of the amplifying electron density peak above $a_{0,\mathrm{L}} = 3.5$, this tuning is limited.

### 3.3. Propagation for longer gas-jets and wavebreaking

Here, we examine the reason for the saturation of energy growth of the sub-cycle pulse for plasmas longer than 30 $\mu$m in figure 3(f). Early in the interaction, figure 8(a), the sub-cycle
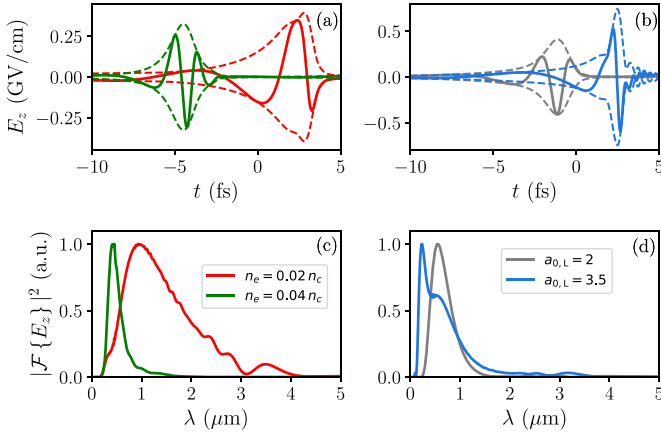
**Figure 7.** Demonstration of the spectral tunability in 2D PIC simulations by modifying (a), (c) electron density from $n_e = 3.35 \cdot 10^{19}$ cm$^{-3} \simeq 0.02$ $n_c$ (red lines) to $n_e = 7.8 \cdot 10^{19}$ cm$^{-3} \simeq 0.04$ $n_c$ (green lines) and (b), (d) driver laser peak electric field from $E_{0,L} = 80$ GV cm$^{-1}$ ($a_{0,L} = 2$, gray lines) to $E_{0,L} = 140$ GV cm$^{-1}$ ($a_{0,L} = 3.5$, blue lines). The other parameters are fixed as for figure 3. The figures present the (a) and (b) on-axis electric fields of the sub-cycle pulses (solid lines) together with their envelopes (dashed lines) after the interaction as well as (c) and (d) their power spectra.

pulse is amplified at the back of the bubble. However, after approximately 20 $\mu$m of propagation the bubble begins to lengthen due to pump intensification induced by relativistic self-focusing [31, 43, 44], eventually leading to wavebreaking after 30 $\mu$m of propagation, see figure 8(b) (observe the difference in maximum field of the driver laser compared to figure 8(a)). After this point amplification ceases, as the density spike amplitude sharply declines. Due to bubble lengthening, the sub-cycle pulse propagates unperturbed inside the bubble (see figure 8(c)), as long as the driver laser remains undepleted. We observe that, while before wavebreaking the sub-cycle pulse transverse length scale is less than a micron (figure 8(a)), after wavebreaking the sub-cycle pulse is transversely guided by the bubble structure at a length scale of about two microns (figure 8(a)). As the sub-cycle pulse exits the plasma through a density downramp, its transverse extent increases further, due to the increase in $\lambda_{pe}$ in the downramp (not shown). This transverse guiding leads to an increase of the pulse source size at the exit of the gas jet. One would thus expect that the refocusing of the sub-cycle pulses after interaction would be experimentally feasible, as was the case for other ultrashort pulses generated and guided within wakefields [26].

For the parameters of the simulation of figure 8, depletion becomes an issue at about 200 $\mu$m of propagation. After depletion, the sub-cycle pulse would propagate in an underdense plasma which, for low-intensity pulses, could lead to compensation of their chirp, see section 3.5 below. For intense sub-cycle pulses, such as in the weakly relativistic regime, non-linear effects could be triggered and thus propagation much longer than the driver depletion length $L_{pd}$ should be avoided.

Bubble lengthening is a relatively slow process, here occurring over $\sim 10$ $\mu$m of propagation. While the bubble lengthens, the density spike at the back of the bubble effectively moves
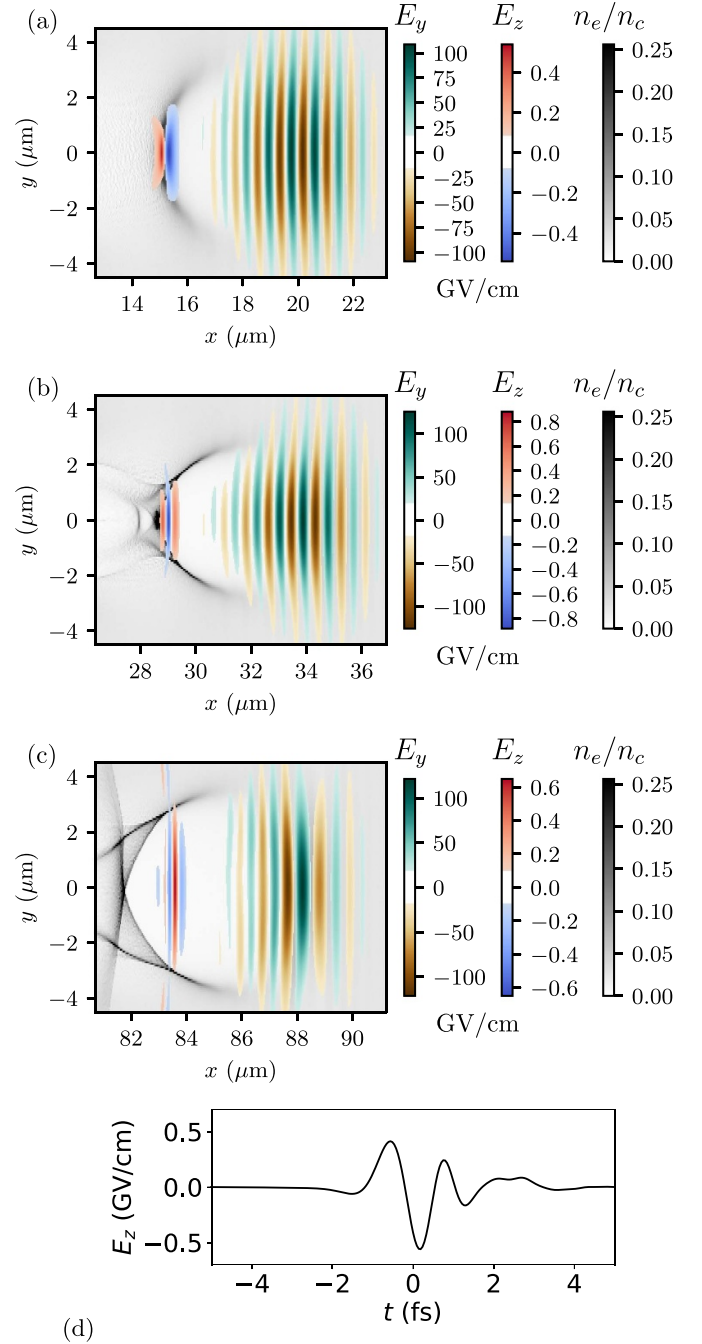


**Figure 8.** Snapshots from 2D PIC simulations (a) before (b) during and (c) after wavebreaking, and (d) the associated sub-cycle signal. The total length of the plasma is $L_p = 24\lambda_{pe} \simeq 120$ $\mu$m while the remaining parameters are the same as figure 3(a).

at lower speed than the front of the bubble. Amplification during bubble lengthening can then result in additional low amplitude oscillations in the sub-cycle pulse, as shown in figure 8. The duration of this pulse has been increased slightly from 0.5 to 0.7 cycles compared to the reference case of figure 3(a). A strategy to prevent pulse lengthening and to increase the effective amplification length would be to adjust the driving laser pulse focusing parameters in order to control self-focusing [43]. A different strategy would be to induce
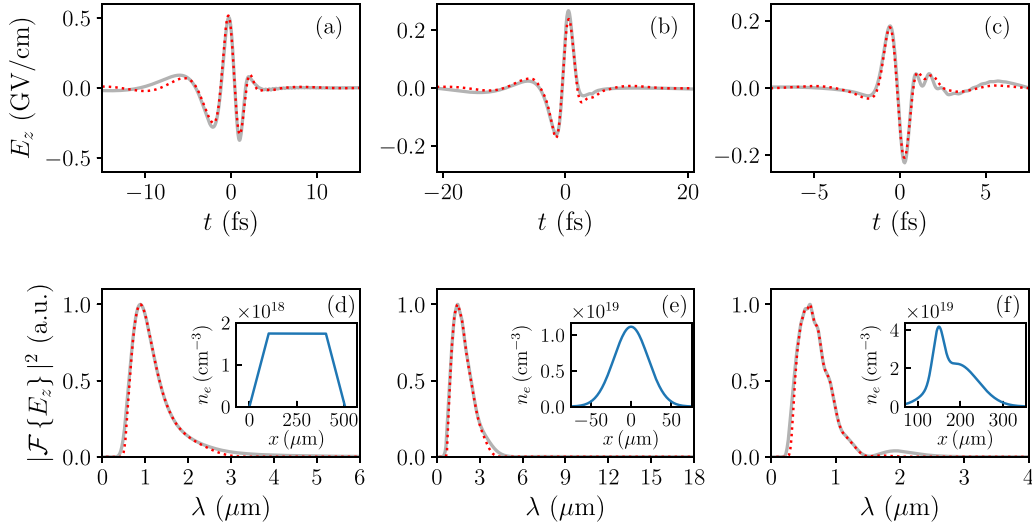
**Figure 9.** Sub-cycle pulses and spectra generated in 2D PIC simulations using ((a) and (d)) linear density up- and down- ramps of $4\lambda_{pe} \simeq 100 \ \mu m$ and a flat top profile of $L_p = 12\lambda_{pe} \simeq 300 \ \mu m$ for $n_0 = 1.7 \cdot 10^{18} \ cm^{-3}$, ((b) and (e)) a Gaussian density profile with FWHM of 50 $\mu m$ for $n_0 = 1.1 \cdot 10^{19} \ cm^{-3}$, ((c) and (f)) a structured target with peak density $n_0 = 4.5 \cdot 10^{19} \ cm^{-3}$. The insets show the plasma density profiles. Solid grey lines are unfiltered pulse fields and spectra at the exit of the gas jet; red dotted lines represent the same after applying a bandpass filter covering 2.5 octaves around the peak wavelength of the subcycle pulse.

wavebreaking at a faster time-scale using tailored density targets, in order to avoid a slow bubble lengthening effect due to relativistic self-focusing. The latter strategy is explored in section 3.4.

### 3.4. Non-homogeneous density profiles and control by density tailoring

In most of our computations we used flat-top density profiles with sharp density transitions, in order to keep the computational domains as compact as possible. Here, we show that the method still works efficiently when the gas-jet density profile is non-homogeneous.

We begin with the case of a 300 $\mu m$ flat-top profile at $n_0 = 1.7 \cdot 10^{18} \ cm^{-3}$ with linear density up and down-ramps of 100 $\mu m$ length, shown in figures 9(a) and (d). We observe a rather minimal lengthening of the pulse duration from 0.8 cycles without the density ramps (not shown) to 0.9 cycles with the density ramps.

For the second example, figures 9((b) and (e)), we consider a Gaussian density profile with FWHM of 50 $\mu m$, i.e. similar to the length-scale reported in recent experiments [49]. We choose peak density $n_0 = 1.1 \cdot 10^{19} \ cm^{-3}$ (0.0064 $n_c$) in order to ensure propagation without wavebreaking until the peak density is reached. We rescale interaction parameters to $\lambda_{pe}^{max} = 10 \ \mu m$ and we use a 7-cycle duration, 50-micron waist seed with 12.5 $\mu m$ central wavelength. Amplification occurs in the rising edge of the gas-jet, where the high-density gradient significantly enhances the leading density spike, while suppressing wavebreaking [52] (see also [27] for a 3D PIC study with similar parameters). Amplification is interrupted shortly after the seed enters the declining part of the Gaussian, due to wavebreaking associated with the downramp [46]. Nevertheless, wavebreaking in this case occurs rapidly and has no

consequence for the duration of the sub-cycle pulse, which is a mere 0.5 cycles at a peak wavelength of 1.45 $\mu m$. We performed additional simulations with this density profile with seed peak amplitudes of up to 1.2 GV cm$^{-1}$ obtaining sub-cycle pulses with peak amplitudes of up to 10 GV cm$^{-1}$ at the exit of the gas-jet, reaching up to 0.5% conversion efficiency (not shown).

For the higher-end of interesting densities, e.g. $n_0 = 4.5 \cdot 10^{19} \ cm^{-3}$, suitable profiles could be produced by density structuring. For the simulation of figure 9(c) a longitudinally tailored density profile of the form

$$n(x,y) = n_0 \left[ c_1 \, e^{((x-x_1)^2/L_1^2)} + c_2 \, e^{-(x-x_2)^2/L_2^2} \right], \quad (5)$$

with $n_0 = 4.5 \cdot 10^{19} \ cm^{-3}$, $c_1 = 0.7$, $c_2 = 0.35$, $L_1 = 17.5 \ \mu m$, $L_2 = 71 \ \mu m$, $x_1 = 151 \ \mu m$ and $x_2 = 194 \ \mu m$ has been used. The FWHM of the longer length-scale, lower density Gaussian is $\sim 120 \ \mu m$ which would be experimentally feasible [47, 49]. The shorter length-scale Gaussian profile was chosen to have FWHM of 6 $\lambda_{pe} \sim 30 \ \mu m$, to ensure propagation without wavebreaking until the density maximum. This profile was inspired by tailored density profiles that have been created by introducing a razor blade in a gas-jet in order to create a local density inhomogeneity [47]. We checked with additional simulations that the details of the profile, for example the sharpness of the downramp transition, are not crucial for our purposes. For the seed laser with $\lambda_S = 4 \ \mu m$ we took 16 $\mu m$ waist and 7-cycle duration, while the rest of the parameters correspond to the reference case of figure 3(a). Similar to the case of figure 9(b), amplification occurs until the peak density is reached, followed by wavebreaking and propagation of the sub-cycle pulse in the elongated bubble, until it exits the plasma. Due to the low plasma density in the second part of the jet, depletion of the pump is avoided. Note that since in
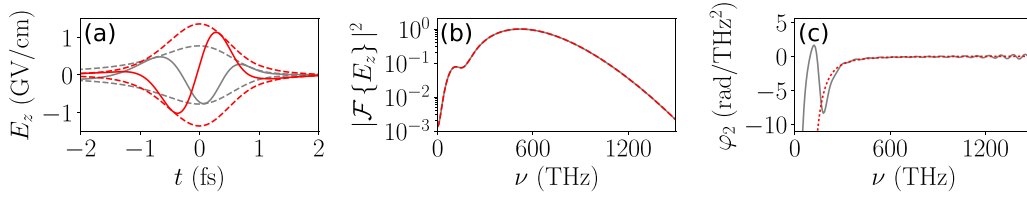
**Figure 10.** Demonstration of the post-compression towards the band-width limit, assuming that the sub-cycle pulse from the 2D PIC simulation of figure 3(b) has been propagating through a 7.5-mm-long low-density plasma with the electron density $n_e = 5 \cdot 10^{16}$ cm$^{-3}$: (a) the original (gray line) and compressed (red line) pulses (solid lines) and their envelopes (dashed lines), (b) corresponding power spectra and (c) the second derivative of the spectral phase (chirp) for the original pulse (solid line) and the negative of the chirp, introduced by the plasma (dashed line), demonstrating an almost perfect compensation of the chirp, resulting in a shorter and 2.5 times more intense bandwidth limited sub-cycle pulse.

figure 9 we show the signal at the exit of the gas-jet, its amplitude is reduced due to diffraction. The pulse has 0.6-cycle duration and peak wavelength of $\sim 0.6$ $\mu$m.

The spectra of the sub-cycle pulses presented here are ultrabroadband and their interpretation requires some care. To this end, we apply spectral filtering to the sub-cycle pulses of figure 9. It is shown that using a bandpass filter to retain approximately 2.5 octaves around the peak wavelength is sufficient in order to reproduce the pulse shapes. Measurement and characterization of sub-cycle pulses within this range of frequencies should be possible with existing equipment [13].

### 3.5. Post-compression towards the bandwidth limit

The pulses produced by LWDA, such as the one in figure 10(a) (gray lines), have an asymmetric envelope. Here we suggest that, after the main interaction, the sub-cycle pulse can be post-compressed through propagation in a low-density plasma. This can occur either through the trapping of the sub-cycle pulse inside the low density plasma in the bubble, induced by wavebreaking, or using a second gas jet of suitable parameters (after collimation of the sub-cycle pulse in order to avoid nonlinear effects). Here, we briefly examine how the parameters of such an interaction can be chosen.

The asymmetry in the envelope of the sub-cycle pulses is intimately linked to the non-vanishing curvature of the spectral phase $\varphi(\omega) = \angle \mathcal{F}\{E_z\}$,

$$\varphi_2(\omega) = \frac{\partial^2 \varphi(\omega)}{\partial \omega^2}. \tag{6}$$

which is also called a chirp (see figure 10(c), solid line). The chirps of the sub-cycle pulses generated by LWDA have a characteristic shape that can be compensated by the group velocity dispersion introduced by a plasma. The latter leads to a chirp $\varphi_{p,2}$ which can be computed as:

$$\varphi_{p,2}(\omega) = \frac{\partial^2 \varphi_p(\omega)}{\partial \omega^2}, \tag{7}$$

where the phase $\varphi_p$ which is accumulated in a plasma of length $L_p$ is

$$\varphi_p = \frac{\omega}{c} L_p n(\omega). \tag{8}$$

Here, $n(\omega)$ is the refractive index for a plasma with a density $n_e$ which can be approximated for $\omega > \omega_{pe}$ by

$$n(\omega) = \sqrt{1 - \frac{\omega_{pe}^2}{\omega^2}}, \tag{9}$$

with angular plasma frequency $\omega_{pe} = \sqrt{q_e^2 n_e / (\epsilon_0 \, m_e)}$. A compensation of the chirp requires that

$$\varphi_2(\omega) \approx -\varphi_{p,2}(\omega) \tag{10}$$

in the frequency range in which most of the spectral power in the sub-cycle pulse is concentrated], see figure 10(c), dotted red line. In practice, we choose a value $\omega_0$ that corresponds to the central frequency of the sub-cycle pulse and a value $n_0$ such that the plasma is underdense for the frequencies of interest and solve equation (10) for $L_p$. For highly underdense plasma, $\omega_{pe}/\omega_0 = n_0/n_c \ll 1$, Equation (10) simplifies to

$$\varphi_2(\omega_0) \approx \frac{L_p}{c \omega_0} \frac{n_0}{n_c}, \tag{11}$$

which shows that one can reduce the plasma length by an arbitrary factor when increasing the plasma density correspondingly. For example, for $n_e = 5 \cdot 10^{16}$ cm$^{-3}$ we obtain $L_p \approx 7.5$ mm, while for $n_e = 5 \cdot 10^{17}$ cm$^{-3}$ we obtain $L_p \approx 750$ $\mu$m. After the post-propagation of the sub-cycle pulse through a low-density plasma, the chirp can be almost removed and the sub-cycle pulse becomes symmetric, shorter and about 2.5 times more intense (see figure 10(a), dark red lines). Note that while we consider the interaction after collimation, in figure 10(a) we plot fields corresponding to re-focusing the sub-cycle pulse for the sake of comparison.

## 4. Conclusions

In summary, we present extensive computational parametric studies of sub-cycle generation through LWDA, showing that the scheme is robust over a wide range of laser and plasma parameters. We place particular emphasis on varying the background plasma density over more than an order of magnitude, allowing the wavelength of the produced sub-cycle pulses to be adjusted from the mid-IR to the UV. Structured density targets can be used in order to provide the short interaction

length required in the high-density regime. Within the parametric range studied, conversion efficiencies are of the order of 0.1%–1%, suggesting the scalability of sub-cycle pulse energies up to 10mJ for Joule-class driver laser pulses.

## Data availability statement

The data that support the findings of this study are available upon reasonable request from the authors.

## Acknowledgments

## ORCID iD

E Siminos   https://orcid.org/0000-0002-1484-0559

## References

[1] Corkum P B and Krausz F 2007 *Nat. Phys.* **3** 381
[2] Schultze M *et al* 2013 *Nature* **493** 75
[3] Krausz F and Stockman M I 2014 *Nat. Photon.* **8** 205
[4] Pupeza I *et al* 2015 *Nat. Photon.* **9** 721
[5] Schubert O *et al* 2014 *Nat. Photon.* **8** 119
[6] Hohenleutner M, Langer F, Schubert O, Knorr M, Huttner U, Koch S W, Kira M and Huber R 2015 *Nature* **523** 572
[7] Krüger M, Schenk M and Hommelhoff P 2011 *Nature* **475** 78
[8] Rybka T, Ludwig M, Schmalz M F, Knittel V, Brida D and Leitenstorfer A 2016 *Nat. Photon.* **10** 667
[9] Kling M F *et al* 2006 *Science* **312** 246
[10] Hernández-García C, Pérez-Hernández J A, Popmintchev T, Murnane M M, Kapteyn H C, Jaron-Becker A, Becker A and Plaja L 2013 *Phys. Rev. Lett.* **111** 033002
[11] Silva F, Teichmann S M, Cousin S L, Hemmer M and Biegert J 2015 *Nat. Commun.* **6** 6611
[12] Manzoni C, Mücke O D, Cirmi G, Fang S, Moses J, Huang S, Hong K, Cerullo G and Kärtner F X 2015 *Laser Photonics Rev.* **9** 129
[13] Liang H *et al* 2017 *Nat. Commun.* **8** 141
[14] Voronin A A and Zheltikov A M 2017 *Sci. Rep.* **7** 36263
[15] Baeva T, Gordienko S and Pukhov A 2006 *Phys. Rev.* E **74** 065401(R)
[16] Tzallas P, Skantzakis E, Kalpouzos C, Benis E P, Tsakiris G D and Charalambidis D 2007 *Nat. Phys.* **3** 846
[17] Yeung M *et al* 2015 *Phys. Rev. Lett.* **115** 193903
[18] Tsakiris G D, Eidmann K, Meyer-ter Vehn J and Krausz F 2006 *New J. Phys.* **8** 19
[19] Heissler P *et al* 2012 *Phys. Rev. Lett.* **108** 235003
[20] Ma G, Dallari W, Borot A, Krausz F, Yu W, Tsakiris G D and Veisz L 2015 *Phys. Plasmas* **22** 033105
[21] Kormin D, Borot A, Ma G, Dallari W, Bergues B, Aladi M, Földes I B and Veisz L 2018 *Nat. Commun.* **9** 4992
[22] Vincenti H and Quéré F 2012 *Phys. Rev. Lett.* **108** 113904
[23] Wheeler J A, Borot A, Monchocé S, Vincenti H, Ricci A, Malvache A, Lopez-Martens R and Quéré F 2012 *Nat. Photon.* **6** 829
[24] Thiele I, Siminos E and Fülöp T 2019 *Phys. Rev. Lett.* **122** 104803
[25] Nie Z *et al* 2018 *Nat. Photon.* **12** 489
[26] Nie Z *et al* 2020 *Nat. Commun.* **11** 2787
[27] Siminos E, Thiele I and Olofsson C 2021 *Phys. Rev. Lett.* **126** 044801
[28] Derouillat J *et al* 2018 *Comput. Phys. Commun.* **222** 351
[29] Thiele I, Skupin S and Nuter R 2016 *J. Comput. Phys.* **321** 1110
[30] Pérez F and Grech M 2019 *Phys. Rev.* E **99** 033307
[31] Sävert A *et al* 2015 *Phys. Rev. Lett.* **115** 055002
[32] Sprangle P, Esarey E and Ting A 1990 *Phys. Rev.* A **41** 4463
[33] Bulanov S V, Kirsanov V I and Sakharov A S 1989 *JETP Lett.* **50** 198
[34] Esarey E, Schroeder C B and Leemans W P 2009 *Rev. Mod. Phys.* **81** 1229
[35] Lu W, Tzoufras M, Joshi C, Tsung F S, Mori W B, Vieira J, Fonseca R A and Silva L O 2007 *Phys. Rev. ST Accel. Beams* **10** 061301
[36] Wilks S C, Dawson J M, Mori W B, Katsouleas T and Jones M E 1989 *Phys. Rev. Lett.* **62** 2600
[37] Esarey E, Ting A and Sprangle P 1990 *Phys. Rev.* A **42** 3526
[38] Oliveira e Silva L and Mendonça J T 1998 *Phys. Rev.* E **57** 3423
[39] Murphy C D *et al* 2006 *Phys. Plasmas* **13** 033108
[40] Bu Z, Shen B, Yi L, Zhang H, Huang S and Li S 2015 *Phys. Plasmas* **22** 043102
[41] Olofsson C 2020 Models of sub-cycle electromagnetic pulse generation in laser-plasma interaction *Master's Thesis* Chalmers University of Technology, Gothenburg, Sweden
[42] Golovin G *et al* 2018 *Phys. Rev. Lett.* **121** 104801
[43] Thomas A G R *et al* 2007 *Phys. Rev. Lett.* **98** 095004
[44] Kalmykov S, Yi S A, Khudik V and Shvets G 2009 *Phys. Rev. Lett.* **103** 135004
[45] Shadwick B A, Schroeder C B and Esarey E 2009 *Phys. Plasmas* **16** 056704
[46] Geddes C G R, Nakamura K, Plateau G R, Toth C, Cormier-Michel E, Esarey E, Schroeder C B, Cary J R and Leemans W P 2008 *Phys. Rev. Lett.* **100** 215004
[47] Schmid K, Buck A, Sears C M S, Mikhailova J M, Tautz R, Herrmann D, Geissler M, Krausz F and Veisz L 2010 *Phys. Rev. ST Accel. Beams* **13** 091301
[48] Buck A *et al* 2013 *Phys. Rev. Lett.* **110** 185006
[49] Faure J, Gustas D, Guénot D, Vernier A, Böhle F, Ouillé M, Haessler S, Lopez-Martens R and Lifschitz A 2018 *Plasma Phys. Control. Fusion* **61** 014012
[50] Gordienko S and Pukhov A 2005 Scalings for ultrarelativistic laser plasmas and quasimonoenergetic electrons *Phys. Plasma* **12** 043109
[51] Woodbury D *et al* 2018 *Opt. Lett.* **43** 1131
[52] Mu J, Li F-Y, Zeng M, Chen M, Sheng Z-M and Zhang J 2013 *Appl. Phys. Lett.* **103** 261114